ANNUAL REVIEWS

Annual Review of Physical Chemistry

Ultrafast Imaging of Molecules with Electron Diffraction

Martin Centurion,[1] Thomas J.A. Wolf,[2] and Jie Yang[3]

[1]Department of Physics and Astronomy, University of Nebraska, Lincoln, Nebraska, USA; email: martin.centurion@unl.edu

[2]Stanford PULSE Institute, SLAC National Accelerator Laboratory, Menlo Park, California, USA; email: thomas.wolf@stanford.edu

[3]Center of Basic Molecular Science, Department of Chemistry, Tsinghua University, Beijing, China; email: jieyang1@tsinghua.edu.cn

Annu. Rev. Phys. Chem. 2022. 73:21–42

First published as a Review in Advance on November 11, 2021

The *Annual Review of Physical Chemistry* is online at physchem.annualreviews.org

https://doi.org/10.1146/annurev-physchem-082720-010539

Keywords

ultrafast electron diffraction, molecular imaging, structural dynamics, molecular dynamics, femtosecond dynamics

Abstract

Photoexcited molecules convert light into chemical and mechanical energy through changes in electronic and nuclear structure that take place on femtosecond timescales. Gas phase ultrafast electron diffraction (GUED) is an ideal tool to probe the nuclear geometry evolution of the molecules and complements spectroscopic methods that are mostly sensitive to the electronic state. GUED is a weak and passive probing tool that does not alter the molecular properties during the probing process and is sensitive to the spatial distribution of charge in the molecule, including both electrons and nuclei. Improvements in temporal resolution have enabled GUED to capture coherent nuclear motions in molecules in the excited and ground electronic states with femtosecond and subangstrom resolution. Here we present the basic theory of GUED and explain what information is encoded in the diffraction signal, review how GUED has been used to observe coherent structural dynamics in recent experiments, and discuss the advantages and limitations of the method.

1. INTRODUCTION

The conversion of light into chemical and mechanical energy at the molecular level plays an essential role in many biological processes such as vision (1), photosynthesis (2), the generation of vitamin D (3), and the photodamage of DNA (4, 5). Furthermore, it is also relevant for applications such as molecular switches and energy storage. After photoexcitation, the absorbed energy can be efficiently channeled to the formation of photoproducts through nuclear motions that take place on ultrafast timescales, to bond breaking and making of new bonds, and to vibrations leading to energy dissipation. The dynamics of the transformation from the excited state to end products is often driven by a complex interplay of electronic and nuclear motions. Understanding these mechanisms requires detailed knowledge of the temporal evolution of the electronic configuration and nuclear geometry of the molecule in the excited electronic states. Experiments capable of capturing the dynamics on the relevant temporal and spatial scales are essential for building accurate predictive models of photochemical reactions. Laser-based spectroscopic methods capture changes in electronic configuration and are only indirectly sensitive to changes in nuclear geometry. Time-resolved spectroscopy has been applied to investigate electronic dynamics on the relevant timescales of femtoseconds to attoseconds (6–8). Diffraction methods are directly sensitive to the molecular structure and so offer complementary information by spatially resolving the nuclear motions. Recently, both ultrafast electron diffraction (UED) and ultrafast X-ray diffraction have demonstrated the capability to resolve structural dynamics on femtosecond timescales (9, 10). We focus here on the work carried out with UED.

Gas phase electron diffraction has been a valuable tool to determine the gas phase structure of molecules for several decades (11, 12). Early time-resolved measurements captured the formation of photoproducts on microsecond and nanosecond timescales (11, 13). The first gas phase ultrafast electron diffraction (GUED) experiments with picosecond resolution were carried out in the 1990s to determine the structure of short-lived intermediate states (14, 15) and later to perform diffraction from aligned molecules (16, 17), although the temporal resolution was not sufficient to capture coherent nuclear motions leading to structural changes. In parallel, UED reached femtosecond resolution in experiments with thin (typically less than 100-nm) solid samples (18, 19). For thick gas phase samples, sufficient spatiotemporal resolution for the observation of coherent molecular geometry changes was only achieved recently through the use of relativistic electron guns with megaelectronvolt energy (MeV-UED) (20, 21). Initial proof-of-principle experiments spatially resolved vibrational and rotational wave packets in diatomics (10, 22). More recent experiments probed reactions in more complex molecules, elucidating the dynamics by spatially resolving the nuclear motions (23–26) and by capturing changes in electronic structure reflected in the inelastic scattering (27).

Here, we first review the basic principles underlying GUED that determine what can be learned from the diffraction data. Then, using specific examples of recent experiments, we explain how GUED has been used to reveal dynamics. Finally, we describe the advantages and limitations of GUED based on fundamental principles and current technology and provide a brief outlook into possible advances of the technique.

2. THEORY OF GUED

In this section, we describe the electron-scattering theory relevant to GUED to clarify what information is contained in the diffraction signal.

2.1. Elastic Electron Scattering from an Arbitrary Potential Field or Charge Distribution

Electron scattering by an arbitrary static potential field $V(\vec{R})$ can be described by a solution of Schrödinger's equation (28). Under the Born approximation, the complex amplitude of the elastically scattered electron wave can be described by (28)

$$f(\vec{s}) = \frac{m}{2\pi\hbar^2}\int \exp\left(-i\vec{s}\cdot\overrightarrow{r'}\right)V\left(\overrightarrow{r'}\right)d^3r', \quad 1.$$

where $\vec{s}$ is the momentum transfer of the scattered electron, m is the mass of the electron, and $\hbar$ is the reduced Planck constant.

The Born approximation assumes that the incident wave is much stronger than the scattered wave or, in other words, that the scattered wave will not be scattered again by the target sample. In the 1930s, for electron kinetic energies of 10 keV or higher, the Born approximation was shown to be typically sufficient to describe experimental results (28). In the 1950s, Schomaker and Glauber (29, 30) showed that for gas molecules with both heavy and light atoms, a first-order correction for the Born approximation is needed in which a phase shift is introduced for each type of atom. This phase shift introduces a few percent correction on scattering amplitude at high values of the momentum transfer s for kiloelectronvolt electrons and becomes smaller for higher energy electrons. In addition, McClelland & Fink (31) explained that the Born approximation itself can be sufficiently accurate for interpreting difference signals, even for kiloelectronvolt experiments. A similar argument can be made for time-resolved experiments. For these two reasons, the Born approximation has so far been found to be sufficiently accurate for MeV-GUED experiments.

Equation 1 shows that the elastically scattered wave function can be represented by a Fourier transform of the electrostatic (Coulombic) potential scalar field. For electron diffraction with high-energy electrons, the dominant electron–matter interaction is Coulombic in nature. Therefore, electron diffraction probes the Coulomb potential of the target system. Assuming the charge distribution of the target system is $\rho(\vec{r})$, the elastically scattered wave $f(\vec{s})$ can be rewritten as (derivation described in the **Supplemental Material**)

Supplemental Material >

$$f(\vec{s}) = \frac{me}{2\pi\varepsilon_0\hbar^2}\frac{1}{s^2}\int \exp\left(-i\vec{s}\cdot\vec{r}\right)\rho\left(\vec{r}\right)d^3r. \quad 2.$$

Equation 2 shows that the elastic electron-scattering amplitude is, with an s^{-2} prefactor, proportional to the Fourier transform of the charge distribution of the target system. Equations 1 and 2 together show that electron diffraction probes the Coulomb potential and, equivalently, the charge distribution of the target system. For GUED, the main experimental observable becomes the change in the diffraction patterns, which probes the change of the Coulomb potential/charge distribution of the target system.

2.2. Elastic and Inelastic Scattering from Atoms

An individual atom consists of one nucleus and one or more electrons. As the length scale of nuclei is in femtometers, for GUED experiments they can be treated as point charges, compared to the extension of the atomic orbitals on the Ångstrom scale. For an atom with atomic number Z and the nucleus located at the origin, the nuclear charge density is given by

$$\rho_N(r) = Ze\delta(\vec{r}), \quad 3.$$

where r is the radial dimension in spherical coordinates. The electron charge density is given by the product of the absolute value squared of the electronic wave function $\varphi_e(\vec{r}_1, \vec{r}_2, \ldots, \vec{r}_Z)$ and the

elementary charge e

$$\rho_e(\vec{r}_1, \vec{r}_2, \ldots, \vec{r}_Z) = -e\left|\varphi_e(\vec{r}_1, \vec{r}_2, \ldots, \vec{r}_Z)\right|^2, \quad 4.$$

where $\vec{r}_i$ is the position vector of the i^{th} electron. Equation 4 shows that the electron charge distribution of an atom is a $3{\cdot}Z$-dimensional function. A common approximation is to use the averaged, radially symmetric one-dimensional (1D) electron distribution $\rho_e(r)$ to replace the real electron distribution $\rho_e(\vec{r}_1, \vec{r}_2, \ldots, \vec{r}_Z)$. This approximation has two drawbacks: (*a*) It ignores the fact that the electrons are avoiding each other spatially, i.e., the correlation effect (although negligible in elastic scattering, correlation effects must be taken into account in inelastic scattering calculations) (32), and (*b*) it ignores the possibility that the potential can be rapidly changing during the scattering process after photoexcitation. This effect is demonstrated theoretically for both electron (33, 34) and X-ray (35–38) scattering for extremely short (typically attosecond) pulses. For existing MeV-UED experiments in which the pulse duration is on the order of 100 fs, this effect is negligible.

The charge distribution under this approximation is given by

$$\rho(r) = Ze\delta(\vec{r}) + \rho_e(r). \quad 5.$$

Substituting Equation 5 into Equation 2 and integrating over the isotropic angular coordinates, we can get the elastic scattering amplitude of individual atoms,

$$f(s) = \frac{me^2}{2\pi\varepsilon_0\hbar^2}\frac{1}{s^2}[Z - F(s)] = \frac{2}{a_0 s^2}[Z - F(s)], \quad 6.$$

where a_0 is the Bohr radius and

$$F(s) = 4\pi\int_0^\infty \rho_e(r)\frac{\sin(sr)}{sr}r^2 dr. \quad 7.$$

Equation 6 is the famous Mott-Bethe formula (39, 40) that describes the atomic form factor (AFF) of electron scattering $f(s)$. Equation 7 describes the AFF of X-ray scattering $F(s)$, which was first derived by Debye (41) in 1915. The AFFs are tabulated in, for example, the International Tables for Crystallography (42). The AFFs for elastic electron scattering can also be calculated using the ELSEPA program (43). Equation 6 shows that the AFF scales with atomic number Z. This dependency, however, becomes weaker than a simple linear scaling when the screening effect of the electron cloud is considered. While this effect means that electron scattering from light atoms is weaker than that from heavier atoms, the relative scattering intensity as a function of Z ratio still favors electron over X-ray scattering. For example, in electron scattering, the cross section of the hydrogen atom is ~4% of the cross section of the oxygen atom, while in X-ray scattering this ratio is only ~0.5%.

The inelastically scattered intensity for individual atoms can be expressed as

$$I_{\text{ine}} = \frac{4}{a_0^2 s^4}S_i(s), \quad 8.$$

where $S_i(s)$ is the inelastic scattering factor for X-rays. Inelastic scattering factors for individual atoms are also computed and tabulated in, for example, Reference 42. The I_{ine} simulation is often based on Hartree-Fock wave functions, which are known to quite significantly overestimate the experimental I_{ine} at small angles (44). This is due to Hartree-Fock methods not accounting for the dynamic electron correlation (45, 46).

2.3. Diffraction from Molecules Under the Independent Atom Model

The independent atom model (IAM) is a simple, yet effective approximation for describing the electron-scattering pattern from molecules. It assumes that the electron distribution in a molecule is the same as if the molecule were made of independent, noninteracting atoms and so can be described by tabulated AFFs. This approximation ignores the changes to the electron distribution due to chemical bond formation.

For a molecule that is comprised of N atoms, the elastic scattering amplitude can be written as

$$f_M(\vec{s}) = \sum_{i=1}^{N} f_i(s) e^{i\vec{s}\cdot\vec{r}_i}, \qquad 9.$$

where $f_i(s)$ is the AFF of the i^{th} atom and is given by Equation 6, and $\vec{r}_i$ is the position vector of the i^{th} atom. The elastic scattering intensity can then be described by (28)

$$I_M(\vec{s}) = \left|f_M(\vec{s})\right|^2 = \left|\sum_{i=1}^{N} f_i(s) e^{i\vec{s}\cdot\vec{r}_i}\right|^2 = \sum_{i=1}^{N}\left|f_i(s)\right|^2 + \sum_{i=1}^{N}\sum_{j=1, j\neq i}^{N} f_i^*(s) f_j(s) e^{i\vec{s}\cdot(\vec{r}_i - \vec{r}_j)}. \qquad 10.$$

For samples in the gas phase, the scattered waves from different molecules do not have a fixed phase relation due to their statistically distributed positions; thus, the overall elastic scattering signal is the incoherent sum over an ensemble of randomly oriented molecules. An angular integral over Equation 10 yields the scattering intensity of the whole ensemble

$$I(s) = \sum_{i=1}^{N}\left|f_i(s)\right|^2 + \sum_{i=1}^{N}\sum_{j=1, j\neq i}^{N} f_i^*(s) f_j(s) \frac{\sin(sr_{ij})}{sr_{ij}} = I_{\text{at}} + I_{\text{mol}}, \qquad 11.$$

where

$$I_{\text{at}}(s) = \sum_{i=1}^{N}\left|f_i(s)\right|^2, I_{\text{mol}}(s) = \sum_{i=1}^{N}\sum_{j=1, j\neq i}^{N} f_i^*(s) f_j(s) \frac{\sin(sr_{ij})}{sr_{ij}}. \qquad 12.$$

Equations 11 and 12 give the IAM representation of a rigid molecule.

Two additional corrections are often used in gas electron diffraction (GED). Firstly, the AFF $f_i(s)$ is real under the first Born approximation but can be complex under the first-order correction

$$f_i(s) = \left|f_i(s)\right| e^{i\eta_i}, \qquad 13.$$

where η_i is the phase shift of the i^{th} atom (29, 30) and can be found in, for example, Reference 47. The second correction is to account for small Gaussian-shaped vibrational bond-length distributions. Assuming the mean square amplitude of the vibration of atom pair ij is l_{ij}, the molecular component of Equation 12 can be rewritten as

$$I_{\text{mol}}(s) = \sum_{i=1}^{N}\sum_{j=1, j\neq i}^{N}\left|f_i(s)\right|\left|f_j(s)\right|\cos(\eta_i - \eta_j)\exp\left(-\frac{1}{2}l_{ij}^2 s^2\right)\frac{\sin(sr_{ij})}{sr_{ij}}. \qquad 14.$$

For the ground state, the term $\exp(-\frac{1}{2}l_{ij}^2 s^2)$ describes a Gaussian-shaped probability density that can be used to model low-amplitude vibrations. For many excited-state photochemical processes, significant structural rearrangement takes place, and the ground-state Gaussian-shaped vibrational wave packet is no longer a valid physical picture. For these processes, the Gaussian distribution is replaced with the explicit shape of the excited-state wave packet, in which the time-dependent distribution of the r_{ij} in Equation 12 is often directly applied. Several concrete examples of excited-state wave packets are presented in Section 3.

2.3.1. Isotropic scattering data processing. In most cases, the target molecules studied by GED and GUED are randomly oriented; thus, the diffraction patterns are isotropic (48, 49). This is by far the most common scenario for the published GED and GUED experiments. In this section, we introduce the standard data processing routine for isotropic scattering data. For simplicity, we ignore the two correction terms in Equation 14 and focus on Equations 11 and 12.

Because I_{mol} in Equation 12 has a nominal s^{-5} dependence, it drops quickly with the increase of s, making the signal level vary over several orders of magnitude in a typical data set. A more suitable representation of the scattering signal is given by the modified scattering intensity $sM(s)$,

$$sM(s) = s\frac{I_{\mathrm{mol}}}{I_{\mathrm{at}}}, \tag{15.}$$

and the real-space pair distribution function (PDF) $P(r)$, which is proportional to the probability of finding an atom pair in any distance r, is given by

$$P(r) = r\int_0^\infty sM(s)\sin(sr)\,ds. \tag{16.}$$

The form of the PDF definition can vary slightly across the literature. Sometimes the Jacobian scaling r is not included, and other times a different scaling of $1/r$ is used. $P(r)$ describes the probability of atom pairs, $P(r)/r^2$ describes the corresponding probability density, and $P(r)/r$ is the most convenient to compute mathematically.

In practice, because no experiment can measure an infinite range in s, we use

$$P(r) \approx r\int_{s_{\mathrm{min}}}^{s_{\mathrm{max}}} sM(s)\sin(sr)\,e^{-\alpha s^2}\,ds, \tag{17.}$$

where $e^{-\alpha s^2}$ is a damping factor that avoids sharp-edged sine-transform effects at the high s end, which is equivalent to a Gaussian smoothing in real space.

For GUED, the focus is typically on the change of the diffraction pattern due to molecular excitation. In the following, we assume that the experiment probes the structure at a fixed time t. In reality, the finite instrument response time introduces time blurring, which can be simulated as incoherent averaging of the diffraction signal in time (50). We thus add the time dependence explicitly to Equations 15 and 17, with the results

$$\Delta sM(s;t) = s\frac{\Delta I_{\mathrm{mol}}(s;t)}{I_{\mathrm{at}}(s)} = s\frac{\Delta I(s;t)}{I_{\mathrm{at}}(s)} \quad \text{and} \tag{18.}$$

$$\Delta P(r;t) \approx r\int_{s_{\mathrm{min}}}^{s_{\mathrm{max}}} \Delta sM(s;t)\sin(sr)\,e^{-\alpha s^2}\,ds. \tag{19.}$$

In Equation 18, we assume that both the elastic atomic scattering intensity I_{at} and the inelastic scattering do not change. This assumption is valid under the IAM. Therefore, an obvious advantage of using the difference signal in comparison to the raw signal is that one no longer needs to separate the I_{mol} from incoherent backgrounds. However, once the effects beyond IAM are taken into account, one can no longer simply ignore the change in the inelastic scattering. These effects are discussed in detail in Section 2.3.

To illustrate the effect of nuclear motion on $\Delta sM(s)$ and $\Delta P(r)$ signals, we use the photodissociation of CF_3I, which is described in more detail in Section 3.2.2. In **Figure 1*a***, we show the

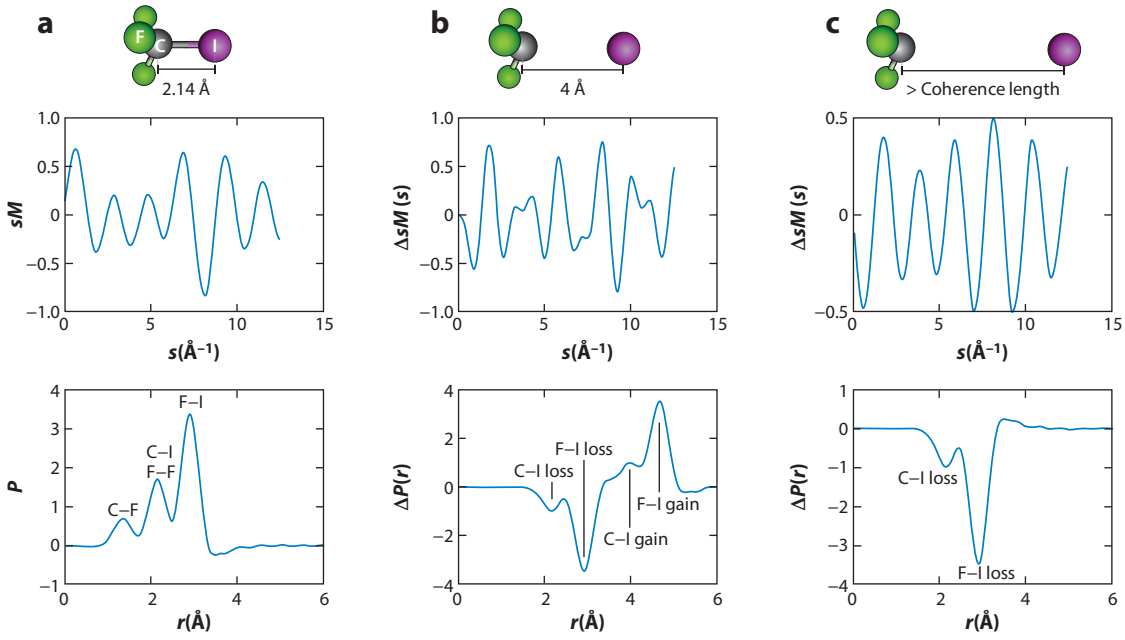

Figure 1

Simulated signal for CF_3I dissociation. (*a*) Ball-and-stick model, the modified scattering intensity $sM(s)$, and the pair distribution function $P(r)$ for the ground-state structure of CF_3I. (*b*) Ball-and-stick model, $\Delta sM(s)$, and $\Delta P(r)$ for a dissociating CF_3I with C–I distance elongated to 4 Å. (*c*) $\Delta sM(s)$ and $\Delta P(r)$ for a dissociating CF_3I with a C–I distance beyond the coherence length of the electron beam. $P(r)$ and $\Delta P(r)$ are calculated using Equations 17 and 19 with $\alpha = 0.02$, $s_{min} = 0$, and $s_{max} = 12.5$ Å^{-1}.

static simulated $sM(s)$ and $P(r)$ of CF_3I at its ground-state equilibrium geometry, at which the C–I distance is 2.14 Å. The atom pair distances are marked in the bottom plot. **Figure 1*b*** shows the $\Delta sM(s)$ and $\Delta P(r)$ for a simplified model of the dissociating CF_3I molecule, assuming that only the iodine atom is moving. The C–I distance is elongated to 4 Å. When the iodine atom moves, both the C–I and the F–I atom pairs move to a larger distance, as marked in the bottom panel in **Figure 1*b***. The motion appears as a set of negative contributions to $\Delta P(r)$ at the equilibrium distances and positive contributions at the new distances. Practically, the positive peaks are always weaker because of wave-packet dispersion, which is not included here. When the C–I distance moves outside the coherence length (typically 1–2 nm for MeV-UED), the interferences between the iodine atom and other atoms are no longer visible, and the only signals remaining visible in $\Delta P(r)$ are the lost original atom pairs, as shown in **Figure 1*c***.

2.3.2. Anisotropic scattering data processing. Under certain circumstances, experiments may disrupt the innate randomness of molecular orientation, thus causing diffraction patterns to no longer be isotropic. Anisotropic molecular orientation (and thus anisotropic diffraction patterns) can be obtained by either actively aligning gas molecules using a femtosecond laser (16, 17, 22, 51) or by photoselection using a linearly polarized excitation laser, in resonance with an electronic excitation (23, 52–55) (see Section 3.1).

Different methods introduce particular angular distributions. In the simplest case, the excited-state molecular ensemble is photoselected by a linearly polarized laser pulse in a single-photon excitation scheme. Under such circumstances, the angular distribution of the excited-state

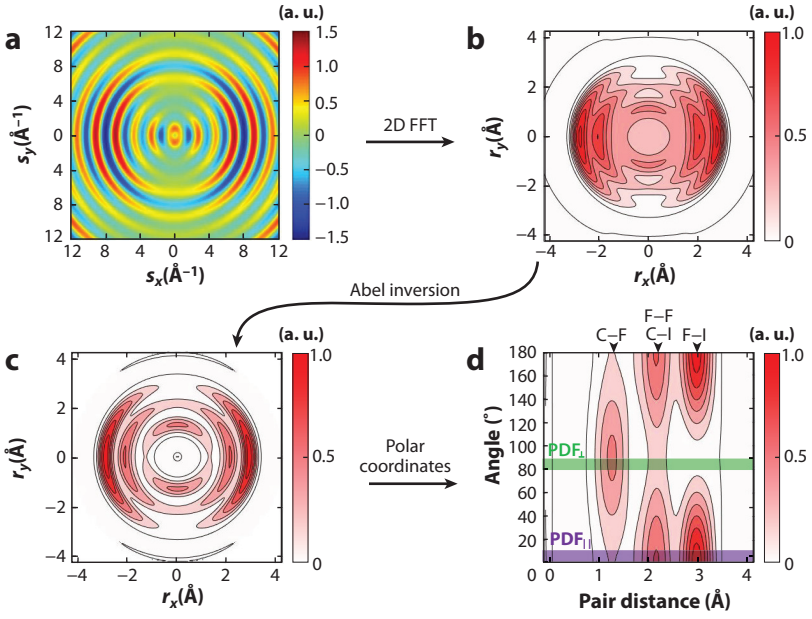

Figure 2

An illustration of the angular-dependent Fourier analysis. (*a*) Simulated diffraction pattern of gas phase CF_3I with a $\cos^2\theta$ angular distribution. (*b*) The two-dimensional (2D) fast Fourier transform (FFT) of panel *a*. (*c*) The angularly resolved pair distribution function (ARPDF), which was obtained by a pBasex Abel inversion of panel *b*. (*d*) The ARPDF represented in polar coordinates. The top arrows mark the positions for different atom pairs. The parallel (*purple stripe*) and perpendicular (*green stripe*) directions show very different PDFs. Figure is adapted with permission from Reference 23.

wave-packet probability density follows a $\cos^2\theta$, while the ground state has a $1 - \kappa\cos^2\theta$ distribution, where θ is the angle between the transition dipole moment (TDM) of the molecule and the laser polarization and κ is the excitation fraction. Each atom pair has its own angular distribution, depending on its relative orientation to the TDM at time zero. A detailed discussion of this phenomenon is given by Baskin & Zewail (52, 53). This angular distribution is transient and will be lost due to rotational dephasing, which is typically on the order of a few hundred femtoseconds to a few picoseconds (53–55). Therefore, an instrumental response function in the femtosecond domain is needed to resolve the anisotropic GUED patterns due to photoselection.

The angularly resolved pair distribution function (ARPDF) can be retrieved by an inverse two-dimensional (2D) Fourier transform followed by an inverse Abel transform that uses the symmetry properties of the setup, as explained in the supplementary material in Reference 23.

An example of retrieving ARPDF from a 2D diffraction pattern using the pBasex algorithm (56) is given in **Figure 2**. **Figure 2*a*** shows a simulated diffraction pattern for an ensemble of isolated CF_3I molecules with a $\cos^2\theta$ angular distribution. Its 2D inverse Fourier transform is shown in **Figure 2*b***, and the ARPDF obtained by Abel inversion is shown in **Figure 2*c***. **Figure 2*d*** shows the ARPDF in polar coordinates, where the C–I and F–I interatomic distances appear preferentially along the parallel direction, and the C–F and F–F distances appear preferentially along the perpendicular direction. This example shows that the anisotropic diffraction pattern contains information about not only the atom pair distances but also their angular distributions.

2.4. Electron Scattering Beyond the Independent Atom Model

Atoms forming a molecule will have valence electrons rearranged in chemical bonds. The IAM ignores the changes in electron distribution due to bond formation. This change can be separated into two parts: the binding effect, which describes the change in the averaged electron density distribution (one-electron effect), and the correlation effect, which describes the change in the electron correlation (two-electron effect) (44, 46). The two terms capture the first- and second-order density matrices of the electronic wave function, respectively (44, 46).

The total and elastic scattering intensity can be written as (32, 57)

$$I_{\text{tot}} = \left\langle \psi_{\text{i}} \left| \hat{L}\hat{L}^{*} \right| \psi_{\text{i}} \right\rangle \text{ and} \tag{20.}$$

$$I_{\text{elastic}} = \left\| \left\langle \psi_{\text{i}} \left| \hat{L} \right| \psi_{\text{i}} \right\rangle \right\|^{2}, \tag{21.}$$

where ψ_{i} is the initial electronic state and $\hat{L}$ is the electron scattering operator given by the equation

$$\hat{L} = \frac{1}{s^2}\left[\sum_{\alpha}^{\text{nuclei}} N_{\alpha} \exp\left(i\vec{s}\cdot\vec{r}_{\alpha}\right) - \sum_{j}^{\text{electron}} \exp\left(i\vec{s}\cdot\vec{r}_{j}\right) \right], \tag{22.}$$

where N_{α} is the number of protons in nucleus α. A similar formula for X-ray scattering was first derived by Waller et al. (58) in 1929 and experimentally demonstrated by Woo (59) in 1930.

Equation 20 requires the scattering operator to be applied twice to the initial wave function, and thus encodes the two-electron property. Using $\rho(\vec{r})$ and $\rho^{(2)}(\vec{r},\vec{r}\,')$ to represent the one-electron and the two-electron reduced density matrix of the target molecule, their corresponding Fourier transforms are

$$F^{(1)}(\vec{s}) = \int e^{i\vec{s}\cdot\vec{r}} \rho(\vec{r})\, d^3r \text{ and} \tag{23.}$$

$$F^{(2)}(\vec{s}) = \int e^{i\vec{s}\cdot(\vec{r}-\vec{r}\,')} \rho^{(2)}(\vec{r},\vec{r}\,')\, d^3r d^3r'. \tag{24.}$$

The elastic and inelastic components of electron scattering can be derived as (see **Supplemental Material**)

Supplemental Material >

$$I_{\text{elastic}} = s^{-4}\left| \sum_{\alpha} N_{\alpha} e^{i\vec{s}\cdot\vec{R}_{\alpha}} - F^{(1)}(\vec{s}) \right|^{2} \text{ and} \tag{25.}$$

$$I_{\text{inelastic}} = s^{-4}\left[N + F^{(2)}(\vec{s}) - \left|F^{(1)}(\vec{s})\right|^{2} \right], \tag{26.}$$

where N is the total number of electrons in the molecule. As N is a constant in a neutral molecule, Equation 26 shows that the inelastic component is governed by the difference between $F^{(2)}(\vec{s})$ and $|F^{(1)}(\vec{s})|^2$. $F^{(2)}(\vec{s})$ represents the reciprocal space distribution of $\rho^{(2)}(\vec{r},\vec{r}\,')$, which gives the probability of finding one electron at position $\vec{r}$ while finding another electron at position $\vec{r}\,'$. Taking the square of Equation 23, $|F^{(1)}(\vec{s})|^2$ can be written as

$$\left|F^{(1)}(\vec{s})\right|^{2} = \int e^{i\vec{s}\cdot(\vec{r}-\vec{r}\,')} \rho(\vec{r})\, \rho(\vec{r}\,')\, d^3r d^3r'. \tag{27.}$$

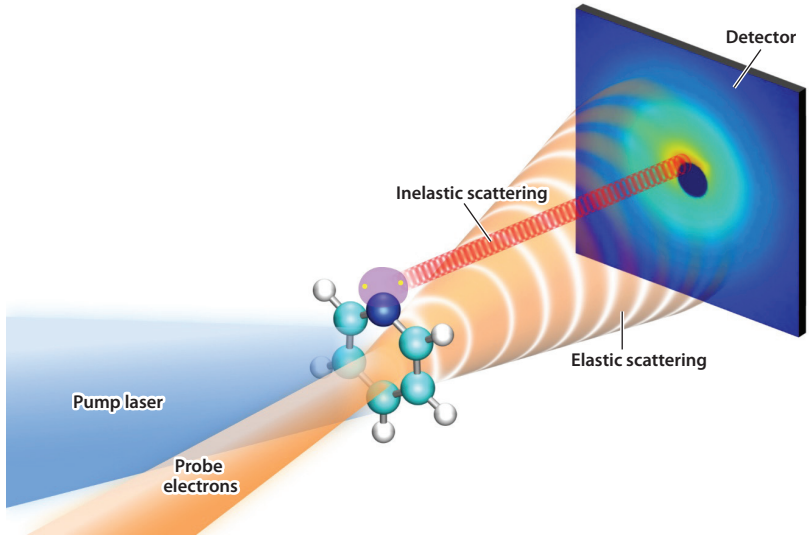

Figure 3

Schematic drawing of a megaelectronvolt ultrafast electron diffraction experiment. Elastic scattering (*orange*) appears in large angles and contains information about nuclear structures, while inelastic scattering (*red*) appears in small angles and contains information about valence electrons. Figure is adapted with permission from Reference 27.

Equation 27 shows that $|F^{(1)}(\vec{s})|^2$ represents the reciprocal space distribution of $\rho(\vec{r})\rho(\vec{r}')$, which gives the probability of finding one electron at position $\vec{r}$ while finding another electron at position $\vec{r}'$, under the assumption that there is no electron correlation at all. Therefore, the difference between $F^{(2)}(\vec{s})$ and $|F^{(1)}(\vec{s})|^2$ encodes the spatial modulation of electrons caused by all forms of electron correlation.

In electron scattering, the inelastic component is confined to small scattering angles; thus, it can be separated from the elastic scattering signal in momentum space. This phenomenon arises from the screening effect, where the $s \to 0$ scattering represents the incident electrons at large impact parameters that have experienced a so-called perfectly screened potential and, thus, $Z\text{-}F(s) \to 0$. However, large s scattering represents incident electrons at small impact parameters, those that have penetrated through most of the electron cloud and experienced a nearly unscreened nuclear potential, and, thus, $Z\text{-}F(s) \to Z$. $I_{\text{inelastic}}$, however, arises only from the electronic component and so is free from the screening effect. Therefore, $I_{\text{inelastic}}$ dominates at small s, while I_{elastic} dominates at large s. The inelastic scattering can be used to capture information on the electronic state of the molecule (27) (see Section 3.2.3). A schematic drawing of simultaneously recording elastic and inelastic components in a MeV-UED experiment is shown in **Figure 3**.

3. EXPERIMENTS AND DATA INTERPRETATION

GUED expands structural methods such as GED to the investigation of structural changes in isolated molecules in real time. The availability of relatively high-brightness, femtosecond electron pulses enables GUED to probe multiple timescales from femtoseconds to nanoseconds and focus on a wide variety of molecules, including weakly scattering targets such as organic molecules exclusively composed of light elements (24). In GUED, a process in a dilute gas is triggered by an ultrashort laser pump pulse and probed by electron diffraction at variable pump-probe delays. The

interaction with the pump pulse deposits energy, for example, by absorption of a photon, selectively in specific electronic, vibrational, or rotational degrees of freedom of the molecular sample, and often yields a nuclear wave packet. The dephasing, rephasing, and decoherence of such wave packets can be followed with GUED in real time. In this section, we describe how GUED can be applied to capture the motion of nuclear wave packets, from simple periodic motions to dynamics in complex potentials.

3.1. Laboratory-Frame Nuclear Motion: Rotational Wave Packets

In impulsive alignment experiments (16, 17, 22, 51, 60), a Raman excitation by a strong, nonresonant, typically linearly polarized and near-infrared ultrashort laser pulse launches a rotational wave packet in an initially isotropic molecular sample leading to transient alignment of the molecule, that is, an increased probability of finding the direction of highest polarizability of molecules to be oriented parallel to the laser polarization axis. Due to the coherent nature of the wave packet and the anharmonicity of the rotational states it consists of, it typically shows short alignment revivals on the picosecond timescale. An electron pulse that is timed with the alignment revival and has a duration on the order of or below the temporal width of the revival probes a sample with an anisotropic orientation distribution, leading to an anisotropic diffraction pattern. The anisotropic diffraction provides information about the relative orientation of atomic pairs in the molecule (see Section 2.3.2). It thus contains structural information beyond the 1D atomic pair distribution function $P(r)$, which can be helpful in retrieval of the three-dimensional molecular structure.

An instructive example demonstrating the concept can be found in Reference 16, where impulsively aligned CF_3I molecules were imaged with UED. In addition to the atomic distances, which were obtained from the PDF, the structural information from the anisotropy of the diffraction pattern provided a measurement of the I–C–F bond angle.

A transient alignment can also be produced by resonant photoexcitation of a transition with a well-defined transition dipole moment (22, 52–55). This effect has been employed in a study of photoexcited CF_3I to separate dynamics in two different excitation channels with different transition dipole moment directions (23) (see Sections 2.3.2 and 3.2.2).

3.2. Relative Nuclear Motion in the Molecular Frame

The field of ultrafast dynamics of electronically excited molecules provides a wide field of application for GUED. Due to the difference in electronic character between the excited state (e.g., a $\pi\pi^*$ state) and the ground state, the shapes of their potentials usually differ, leading to a vibrational Franck-Condon progression in absorption spectra, which is the steady-state analogy of a vibrational mode driving a wave packet repeatedly back into the Franck-Condon region. Photoexcitation with a (typically broadband) femtosecond pulse coherently populates several vibrational levels in the excited state, which leads to formation of a vibrational wave packet, analogous to the rotational wave packet launched by transient alignment examples discussed in Section 3.1.

3.2.1. Vibrational wave packets in bound potentials. Small molecules with bound potentials and long excited-state lifetimes exhibit long-lasting vibrational wave-packet signatures. Such wave-packet dynamics have been observed using, for example, all-optical pump-probe spectroscopy in the iconic experiment on NaI by the Zewail group (61). However, mapping of the spectroscopic observable onto the interatomic distance requires prior knowledge of the involved electronic potentials. As demonstrated in Reference 10, UED is capable of directly determining the internuclear separation of the nuclear wave packet as it evolves on the excited-state potential

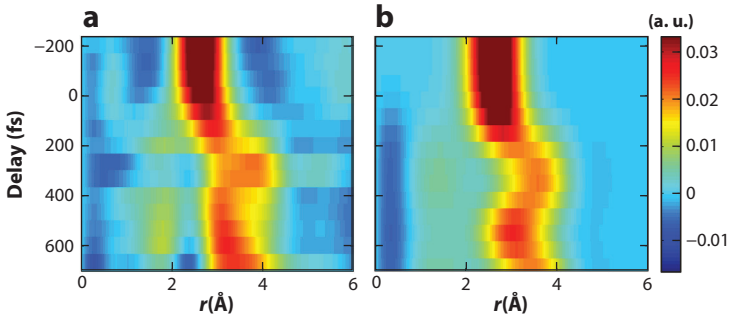

Figure 4

(*a*) Experimental and (*b*) simulated time-resolved atomic pair distribution function from imaging vibrational wave-packet dynamics in photoexcited I_2. For more details on this experiment, see Reference 10.

of I_2 in time and space (see **Figure 4**). The time-dependent center and width of the wave packet can be directly extracted from the diffraction patterns by sine transformation into PDFs.

3.2.2. Wave packets in repulsive potentials. A nuclear wave packet launched on the excited-state surface of a molecule can encounter a repulsive potential. A good example is the excited-state dynamics of CF_3I as investigated by GUED in Reference 23. The excited state of CF_3I, the so-called A-band, which can be reached at an excitation wavelength of 266 nm, is repulsive with respect to C–I bond dissociation. Thus, the excited-state wave packet is immediately accelerated on the bond dissociation coordinate and stays relatively compact in this degree of freedom. The speed of the dissociating wave packet poses challenges to the time resolution of UED in this case. Therefore, the dissociating wave packet itself could not be followed in detail in Reference 23. However, the loss of the strong spatial frequency components from the C–I and F–I equilibrium distances is observable in the diffraction patterns at time zero, which transforms into a bleach of the distances in the difference (Δ) PDFs. Moreover, the dissociation reaction has a secondary effect on the structural dynamics of the CF_3 fragment: The recoil from the dissociation pushes the carbon atom, which has low mass in comparison to the iodine atom, into the F_3 moiety; that is, it excites the umbrella degree of freedom of the CF_3 fragment. Additionally, an increase in the C–F distance upon C–I dissociation could be observed, making CF_3I an example in which GUED images energy flow from a specific excited nuclear degree of freedom into a bath consisting of the remaining degrees of freedom.

3.2.3. Nonadiabatic wave-packet dynamics. In many cases, an excited-state wave packet enters within only a few tens of femtoseconds an area of strong nonadiabatic coupling in the vicinity of a conical intersection (CoIn), a degeneracy between the potential energy surfaces of different electronic states (62, 63). The nonadiabatic coupling can efficiently transfer the wave packet onto a lower-lying potential energy surface, often the electronic ground state. Electron and nuclear motion, which are treated separately within the Born-Oppenheimer approximation, are correlated in the vicinity of CoIns. In cases such as the initial process of human vision in retinal (1), the photoexcited population gains access to new energy minima after relaxation to the ground-state potential energy surface. Relaxation into such minima could establish permanent structural changes and, thus, a photochemical reaction. Many pump-probe spectroscopic methods have been established to investigate such dynamics. However, most of these methods are considerably less sensitive to

structural dynamics than is GUED, as they are based on light interacting with the electrons, not the nuclei of a molecule. Methods such as GUED therefore generally yield complementary information to spectroscopy experiments. In the following subsections, we highlight strengths and weaknesses of UED as a probe for specific aspects of nonadiabatic dynamics.

3.2.3.1. Photoexcitation. Because visible and ultraviolet light purely interact with the valence electrons of a molecule, for example, by promoting an electron from a π orbital to a π^* orbital, no direct signature from the pure photoexcitation, neglecting any nuclear geometry changes, can be expected in GUED data within the IAM. However, as pointed out in Section 2.4, high-energy electrons can interact with the bound electrons of a molecule through inelastic scattering and thus exhibit sensitivity to the electron density distribution, which is altered during photoexcitation. A recent study (27) indeed observed a sizable effect directly connected to the electronic change from photoexcitation. The fact that inelastic scattering signatures are confined to small scattering angles (less than 2 $Å^{-1}$) makes signatures from electronic excitation easily separable from structural dynamics signatures. It is, therefore, well suited to synchronize GUED data sets with, for example, complementary time-resolved spectroscopic measurements.

3.2.3.2. Wave-packet evolution in the excited state toward a conical intersection. An excited-state wave packet often gains access to a CoIn from the Franck-Condon point through a small set of molecular degrees of freedom. A detailed understanding of photochemical reaction mechanisms can be achieved by identifying these modes. Due to its direct structural sensitivity, GUED can be very sensitive to such modes. An instructive example is the electrocyclic ring-opening reaction in the molecule 1,3-cyclohexadiene (CHD) (24). According to quantum chemical simulations, the photoexcited nuclear wave packet first evolves along Franck-Condon active bond alternation modes in a bound potential. Exploring the excited-state potential further, it starts to evolve along a specific degree of freedom separating the two sp^3-hybridized carbons in the ring, which has only a moderate gradient in the excited state. At a carbon–carbon distance of ~2.2 Å, the wave packet encounters a CoIn with the electronic ground state. The wave-packet evolution in this degree of freedom was directly followed in a GUED experiment (24).

3.2.3.3. Wave-packet dynamics at and after access of a conical intersection. When entering a region on the excited-state potential energy surface with large nonadiabatic coupling, complex dynamics can take place governed by the correlated motion of electrons and nuclei. Relaxation through a CoIn typically changes the electronic character of the populated state instantaneously. This instantaneous character change can be tracked in the inelastic scattering signal, as described in Section 2.3.1.

The change in electronic character is often, specifically in the case of CoIns with the ground state, associated with a drastic change in the gradients of the electronic potential the nuclear wave packet experiences. CoIns between excited states and the ground state of organic molecules are usually much closer in potential energy to the Franck-Condon point than to the ground-state minimum. Thus, the nuclear wave packet often experiences a steepening of the potential gradient following internal conversion to the electronic ground state, which leads to wave-packet acceleration. Such an effect could be observed during the ring-opening dynamics of CHD (see **Figure 5**) (24). The molecule requires about 70 fs to increase the C–C distance at the opening position of the ring to 2.2 Å, the value at which it undergoes internal conversion. The distance subsequently increases to 6 Å on a substantially smaller timescale, which could not be quantified further in the experiment due to insufficient temporal resolution.

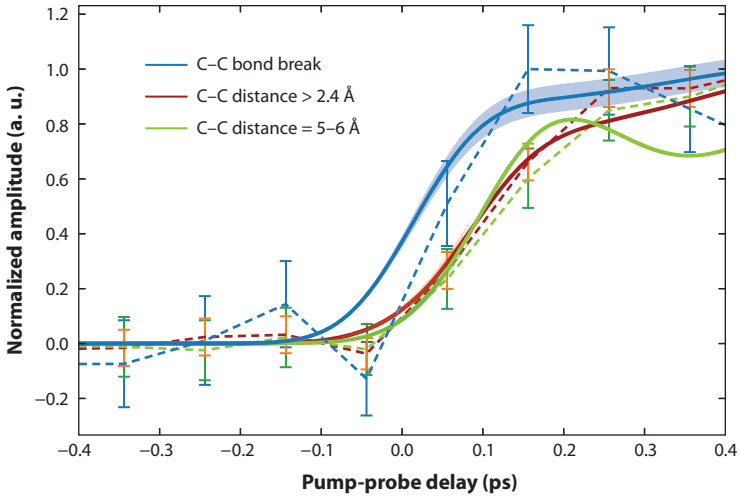

Figure 5

Time dependence of amplitude changes in different areas of simulated (*solid lines*) and experimental (*dashed lines*) difference pair distribution functions (ΔPDFs) of 1,3-cyclohexadiene (for details see Reference 24). The carbon–carbon distance of the dissociating bond grows from 1.4 Å to 2.4 Å within 70 fs, which is evident from the delay between the blue and the orange curves. The internal conversion into the ground state occurs at ∼2.2 Å and leads to a quasi-instantaneous steepening of the potential. This is shown by the fact that no delay in onset is observable between the transient ΔPDF signatures at 2.4 Å (*red*) and 5–6 Å (*green*).

3.2.3.4. Wave-packet bifurcation. UED is, in principle, an ideal tool to observe and identify wave-packet bifurcation into different channels due to its general sensitivity to structural dynamics and subangstrom spatial resolution. However, the ability to distinguish different structural dynamics channels at a given signal-to-noise ratio (SNR) is dependent on their relative quantum efficiency and the relative size of the structural change. The CoIn of CHD is, for example, close to the transition state along the ring-opening reaction coordinate in the ground state. Thus, the wave packet bifurcates in the ground state after internal conversion. About half of the population returns to the CHD ground-state minimum, while the other half relaxes toward the minima of the ring-opened photoproduct. However, the population in the ring-opening direction undergoes a much larger structural change than does the population that returns to the CHD ground-state minimum. Therefore, the part of the population undergoing ring opening is strongly visible in difference-diffraction data. The dynamics leading back to the CHD minimum could not be extracted. A counterexample is found in the relaxation of CF_3I, in which the wave-packet splitting after traversing a CoIn could be resolved with UED (23). In this case, two different excitation channels (single photon versus two photon) were resolved by analyzing the signal's temporal, spatial, and angular dependence.

3.2.3.5. Wave-packet dynamics in the electronic ground state. As discussed in Section 3.2.3.3, relaxation through a CoIn into the ground state typically places the wave packet at a position on the ground-state potential energy surface with a high amount of potential energy and a steep gradient. Thus, the majority of the photoabsorbed energy is released on the ground-state potential energy surface and along the gradient. Hence, the nuclear wave packet arrives at the ground-state minimum of the photoproduct with an extreme amount of nuclear kinetic energy in a single degree or a few internal degrees of freedom. This can launch a vibrational wave packet on the

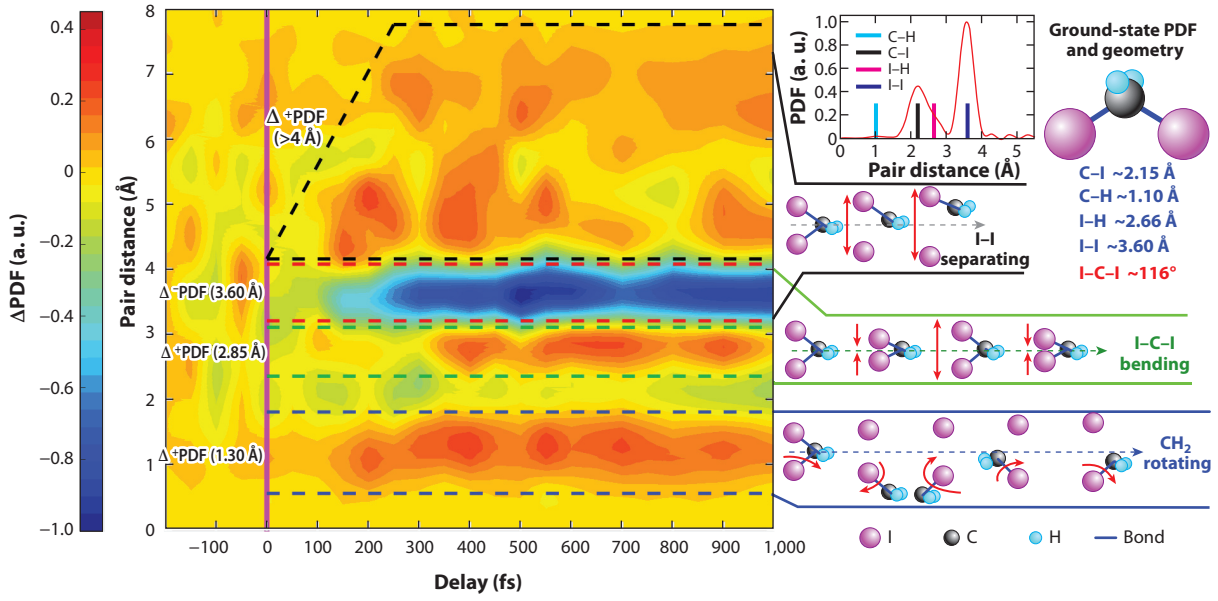

Figure 6

Visualization of several relaxation channels and coherent motions triggered by optical excitation of CH_2I_2, which can be observed in difference pair distribution functions (ΔPDFs) from ultrafast electron diffraction. Photoexcitation can lead to C–I bond dissociation (negative signature at 3.5 Å and positive signature at >4 Å). The dissociation also triggers a rotational motion of the CH_2 group around the remaining iodine atom (signature at ~1 Å). Moreover, signatures from I–C–I bending in a separate, nondissociative channel are visible at ~2.8 Å. Figure adapted with permission from Reference 26.

ground-state surface, similar to the one described in Section 3.2.1 for a photoexcited state of I_2. In the photoproduct of CHD, hexatriene, the ring-opening motion transforms on the ground state into a coherent rotation of the ends of the carbon chain around their bonds with the center of the chain. The projection of this rotation onto the atomic distances is observable in the diffraction data.

Similar coherent wave-packet motion has also been observed in an investigation of the photodissociation dynamics in CH_2I_2 (26). In analogy to the case of CF_3I, photoexcitation leads to dissociation of one of the C–I bonds in the molecule. However, because the breaking chemical bond does not coincide with the rotation symmetry axis of CH_2I_2, it rather triggers rotational motion of the CH_2 moiety around the remaining, substantially heavier iodine atom (see **Figure 6**).

Another example of coherent wave-packet motion is the investigation of the photodissociation of $C_2F_4I_2$ (25). After an early investigation with GUED with picosecond resolution (15), it remained an open question whether, immediately after photodissociation of a C–I bond, the molecule would assume a bridge-like geometry in which the remaining iodine atom would assume similar distances to both carbon atoms or a geometry in which it is still clearly associated with one of the carbons. The GUED investigation in Reference 25 clearly shows that the molecule assumes the latter geometry within 200 fs after photoexcitation. The study further reveals that the excess part of photoabsorbed energy, which is not spent for the bond dissociation, is deposited into coherent oscillations of the remaining C–I and C–F bonds in the molecule.

The transition from such nonstatistical nuclear wave-packet dynamics toward both statistical, microcanonical distribution of the photoabsorbed energy and further ground-state reaction products on the nanosecond and microsecond timescales has not been fully addressed by

time-resolved methods with direct structural sensitivity. Pioneering work has been performed by the Zewail and Weber groups on the picosecond timescale (see, e.g., References 49 and 64). However, the connection to subpicosecond nonequilibrium dynamics and nanosecond and millisecond ground-state reaction kinetics has so far not been fully established.

4. ADVANTAGES AND LIMITATIONS OF GUED

In this section, we discuss the advantages and limitations of GUED, which stem from both the fundamental properties of electron scattering and current technological limitations.

4.1. Fundamental Properties

As described in Section 2, the interaction of the electrons with the sample determines what type of information can be gained from the diffraction patterns. Here we describe the direct structural sensitivity of GUED, how averaging over structures and orientations affects the information content of the diffraction signal, and the advantages of using a weak and passive probe.

4.1.1. Direct structural sensitivity. A major advantage of diffraction measurements is that they can be interpreted in real space by a Fourier analysis of the diffraction patterns, which makes GUED an ideal complement to spectroscopic measurements that probe changes in electronic states. By interpreting the diffraction signal in real space, changes at specific interatomic distances can be accessed directly. These changes can reveal both qualitative and quantitative signatures of specific transformations such as ring opening (the appearance of larger distances), coherent vibrations of a specific bond (periodic modulation of a specific distance in the PDF), and dissociation (fast-increasing distance), along with other motions that can be associated with changes at specific distances.

4.1.2. Signal averaging over structures and orientations. The measured signal is an average over all the different structures that exist at a given time and the angular distribution of the molecules. GUED is thus better suited to detecting the main reaction channels and may struggle to capture minor channels. If the relaxing molecular wave packet remains compact during the relaxation, GUED can, in principle, be used to retrieve the time-dependent structure. If multiple structures exist simultaneously and/or the wave packet spreads significantly, the diffraction signal can be complemented by other measurements such as momentum-resolved coincidence time-of-flight ion mass spectroscopy (65) and/or simulations to retrieve the structures. Additional information can sometimes be retrieved from anisotropic diffraction signals for the case in which the molecules are not randomly oriented, for example, due to the photoselection rules of the excitation (see Sections 2.3.2 and 3.1).

4.1.3. GUED as a weak probe. GUED does not significantly disturb the system being investigated. This is a significant advantage when compared to methods that rely on strong fields such as light-induced electron diffraction (66–68). The interaction of the scattering electron with the molecule does not affect the dynamics and can be simulated accurately using ab initio methods or the IAM, depending on the application.

4.1.4. GUED as a passive probe. GUED is not subject to selection rules, and the elastic scattering cross section can be assumed to be independent of the electronic state of the molecule. This is a significant advantage compared to laser-based methods, in which the initial and final states during the probing need to be known to interpret the data. For laser-based methods that rely on ionization, the ionization cross section may vary depending on the electronic state and

nuclear geometry of the molecule, which makes assigning absolute or even relative weights to different channels difficult.

4.2. Current Technological Limitations

The temporal resolution, spatial resolution (q-range accessible), signal levels, and sample requirements are determined by the current technology in lasers, electron guns, synchronization electronics, and sample delivery.

4.2.1. Temporal resolution. The best demonstrated temporal resolution of GUED experiments is currently ~150 fs for the MeV-UED instrument at the SLAC National Accelerator Laboratory (21, 25). Relative delays between different motions, indicating the sequence of events during a structural transformation, can typically be measured with a resolution significantly below this value due to different signatures in real space for high SNR levels (see the example of CHD in Section 3.2.3). The main factors limiting the temporal resolution are the Coulomb forces that broaden the electron pulses and the timing jitter between the pump laser and probe electrons. As described in Section 3, GUED has successfully captured several types of reactions and nuclear motions. Further improvements in temporal resolution are needed to capture faster dynamics involving the motion of light atoms and transformations that take place on the excited state in shorter times. The temporal resolution is far from any fundamental limits and can be expected to improve significantly over the next few years. There are several ongoing promising efforts in reducing the temporal resolution of MeV-UED (69, 70), compressing electron pulses to 10 fs (71), and improving the resolution in tabletop kiloelectronvolt GUED setups (51, 72). Ultimately, a resolution below 20 fs would be sufficient to capture most relevant nuclear motions.

4.2.2. Spatial resolution and sample requirements. The spatial resolution, signal level, and sample requirements are intertwined. The de Broglie wavelength of megaelectronvolt electrons is typically less than 0.01 Å; thus, it is not the limiting factor for spatial resolution. The spatial resolution is determined by the maximum value of momentum transfer s with sufficient SNR that is captured by the experiment. GUED experiments currently capture a maximum momentum transfer of approximately 10 $Å^{-1}$, which, when converted to a PDF, produces peaks with a width of about 0.6 Å in real space. Changes in distances have been determined with uncertainties below 0.02 Å through shifts in the position of the peaks (23). The differential scattering cross section decreases rapidly with momentum transfer (see Section 2.3.1); thus, the accessible momentum range is usually limited not by detector size but by the current of scattered electrons. This current is proportional to the scattering cross section of the molecule, the current of the incident electron beam, and the column density of the sample (the gas density integrated over the length of the sample). **Figure 7** shows approximate beam current requirements based on the sample column density (number density multiplied by the thickness of the gas beam), assuming a linear increase in beam current to compensate for lower sample density. The required beam current is calculated assuming sufficient data to resolve dynamics at specific interatomic distances and an integration time of 1 h per data point (1 day for a time scan of 24 points), based on the data reported in Reference 24, in which the sample column density was 9×10^{14} molecules/cm^2, the incident beam current was 0.24 pA, and the acquisition time was approximately 1 h per data point. Experiments carried out with parameters that fall below the line in **Figure 7** will be very challenging or not feasible.

GUED experiments currently use slow detectors that average the signal from multiple shots and rely on the conversion of electrons to light for detection. With improved detection systems with the capability to record each event with single-electron sensitivity, the required beam current and/or acquisition time is expected to drop significantly, moving the boundary further down.

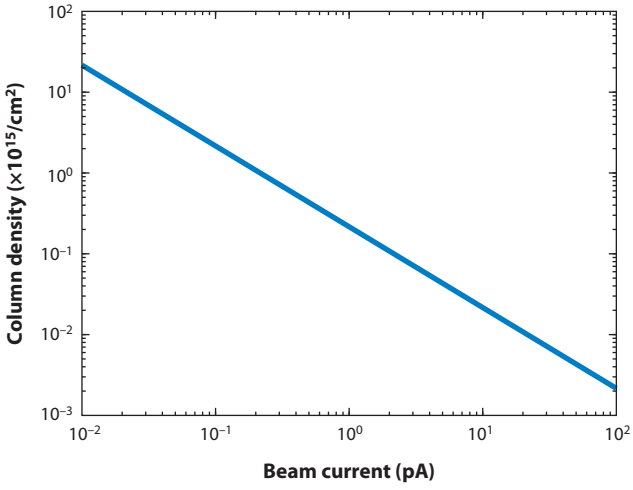

Figure 7

Average incident electron beam current versus sample column density. The beam current is the value required for a time-resolved experiment to reach subangstrom resolution and be carried out with one day of data acquisition time. Data from Reference 24.

4.2.3. Sample delivery. Improvements are also possible in sample delivery to increase the sample density, where the fact that both the electron gun and the detector are far away from the sample region provides a lot of flexibility in the design and use of different technologies.

In summary, GUED is directly sensitive to spatial distribution of charge and thus provides complementary information to spectroscopic measurements that probe electronic energy levels. Because GUED is a weak and passive probe, the signal can be simulated using relatively simple models that greatly aid in data interpretation and comparison with theory. The GUED signal is an ensemble average over a large number of molecules and is therefore better suited to capturing the major reaction channels than to distinguishing channels and products with a low relative yield. One of the limitations of GUED is that it requires a relatively high sample density, although this constraint could be significantly diminished by increasing the incident electron beam current using existing technology for high-repetition-rate electron guns. At present, the temporal resolution is sufficient to capture large structural motions but the faster dynamics involving light atoms are beyond reach.

5. OUTLOOK

Many of the GUED capabilities demonstrated so far are still challenging within the currently available time resolution. It would, for example, be desirable to capture the dissociating wave packet in CF_3I or to more clearly distinguish timescales of electronic and structural change. The current state of the art limits GUED to the study of high vapor pressure model molecules such as CHD, while biorelevant molecules such as provitamin D remain out of reach due to their low vapor pressure. However, we expect that the fast pace of advancing technology will likely result in significant improvements in temporal resolution and electron beam current in the near future. Thus, GUED is well positioned to continue to make a significant impact in ultrafast molecular science. The incident electron beam current can be increased by two or three orders of magnitude using a high-repetition-rate electron gun (73, 74). This will require a parallel increase in laser power to maintain the laser fluence required to excite the sample, but an increase in repetition rate

from existing guns, which operate at around 100 Hz, to 100 kHz is within the realm of existing laser technology. This same technology is already being implemented in next-generation free-electron lasers such as the LCLS (Linac coherent light source) II (75). The charge per pulse could also be increased by an order of magnitude or more using radio frequency fields to compress the duration of the electron pulses at the sample (71, 76), which compensates for space charge forces. Overall, an increase in the electron beam current of between two to four orders of magnitude is possible over the next few years. In addition, recent advances in electron guns and beamline design, along with synchronization electronics, have resulted in significant improvements in MeV- and keV-UED temporal resolution (69, 70, 72). Recent experiments and theory have shown that GUED can capture changes in electronic state in addition to nuclear rearrangements (27), and that it can be applied to study dynamics induced by ionization (65). These advances, coupled with increased beam current, improved temporal resolution, direct electron detection, and availability of the technology to the broader community through user facilities, are expected to greatly enhance the reach and impact of GUED over the next few years.

SUMMARY POINTS

1. Gas phase ultrafast electron diffraction (GUED) captures photoinduced molecular structural changes with high spatial and temporal resolution.
2. GUED is sensitive to changes in the distance and angular distribution of atom pairs in the molecules.
3. The elastic scattering signal reveals the nuclear positions, while the inelastic scattering contains information on the electronic structure.
4. GUED is a weak and passive probe: It does not disturb the system being studied and it scatters from all the structures present in the sample.
5. GUED has been used to observe coherent nuclear motion, including the nonadiabatic splitting of a nuclear wave packet and ring-opening reactions.

DISCLOSURE STATEMENT

The authors are not aware of any affiliations, memberships, funding, or financial holdings that might be perceived as affecting the objectivity of this review.

ACKNOWLEDGMENTS

We thank Markus Guehr and J. Pedro Nunes for reviewing this manuscript. M.C. was supported by the US Department of Energy (DOE) Office of Science, Basic Energy Sciences, Chemical Sciences, Geosciences, and Biosciences Division, AMOS program, under award DE-SC0014170. T.J.A.W. was supported by the US DOE, Office of Science, Basic Energy Sciences, Chemical Sciences, Geosciences, and Biosciences Division.

LITERATURE CITED

1. Polli D, Altoè P, Weingart O, Spillane KM, Manzoni C, et al. 2010. Conical intersection dynamics of the primary photoisomerization event in vision. *Nature* 467:440–43
2. Cheng Y-C, Fleming GR. 2009. Dynamics of light harvesting in photosynthesis. *Annu. Rev. Phys. Chem.* 60:241–62

3. Havinga E, Schlatmann JLMA. 1961. Remarks on the specificities of the photochemical and thermal transformations in the vitamin D field. *Tetrahedron* 16:146–52
4. Schreier WJ, Schrader TE, Koller FO, Gilch P, Crespo-Hernández CE, et al. 2007. Thymine dimerization in DNA is an ultrafast photoreaction. *Science* 315:625–29
5. Wolf TJA, Myhre RH, Cryan JP, Coriani S, Squibb RJ, et al. 2017. Probing ultrafast $\pi\pi^*$ /$n\pi^*$ internal conversion in organic chromophores via K-edge resonant absorption. *Nat. Commun.* 8:29
6. Zewail AH. 2000. Femtochemistry: atomic-scale dynamics of the chemical bond using ultrafast lasers (Nobel lecture). *Angew. Chem. Int. Ed.* 39:2586–631
7. Stolow A, Bragg AE, Neumark DM. 2004. Femtosecond time-resolved photoelectron spectroscopy. *Chem. Rev.* 104:1719–58
8. Krausz F, Ivanov M. 2009. Attosecond physics. *Rev. Mod. Phys.* 81:163–234
9. Minitti MP, Budarz JM, Kirrander A, Robinson JS, Ratner D, et al. 2015. Imaging molecular motion: femtosecond X-ray scattering of an electrocyclic chemical reaction. *Phys. Rev. Lett.* 114:255501

10. Proof-of-principle GUED experiment that captured a vibrational wave packet with atomic resolution.

10. Yang J, Guehr M, Shen X, Li R, Vecchione T, et al. 2016. Diffractive imaging of coherent nuclear motion in isolated molecules. *Phys. Rev. Lett.* 117:153002

11. Ischenko AA, Golubkov VV, Spiridonov VP, Zgurskii AV, Akhmanov AS, et al. 1983. A stroboscopical gas-electron diffraction method for the investigation of short-lived molecular species. *Appl. Phys. B* 32:161–63
12. Mitzel NW, Rankin DWH. 2003. SARACEN – molecular structures from theory and experiment: the best of both worlds. *Dalton Trans.* 19:3650–62
13. Ewbank JD, Luo JY, English JT, Liu R, Faust WL, Schafer L. 1993. Time-resolved gas electron diffraction study of the 193-nm photolysis of 1,2-dichloroethenes. *J. Phys. Chem.* 97:8745–51
14. Williamson JC, Cao J, Ihee H, Frey H, Zewail AH. 1997. Clocking transient chemical changes by ultrafast electron diffraction. *Nature* 386:159–62
15. Ihee H, Lobastov VA, Gomez UM, Goodson BM, Srinivasan R, et al. 2001. Direct imaging of transient molecular structures with ultrafast diffraction. *Science* 291:458–62
16. Hensley CJ, Yang J, Centurion M. 2012. Imaging of isolated molecules with ultrafast electron pulses. *Phys. Rev. Lett.* 109:133202
17. Yang J, Beck J, Uiterwaal CJ, Centurion M. 2015. Imaging of alignment and structural changes of carbon disulfide molecules using ultrafast electron diffraction. *Nat. Commun.* 6:8172
18. Germán S, Miller RJD. 2011. Femtosecond electron diffraction: heralding the era of atomically resolved dynamics. *Rep. Prog. Phys.* 74:096101
19. Siwick BJ, Dwyer JR, Jordan RE, Miller RJD. 2003. An atomic-level view of melting using femtosecond electron diffraction. *Science* 302:1382–85
20. Weathersby SP, Brown G, Centurion M, Chase TF, Coffee R, et al. 2015. Mega-electron-volt ultrafast electron diffraction at SLAC National Accelerator Laboratory. *Rev. Sci. Instrum.* 86:073702
21. Shen X, Nunes JPF, Yang J, Jobe RK, Li RK, et al. 2019. Femtosecond gas-phase mega-electron-volt ultrafast electron diffraction. *Struct. Dyn.* 6:054305

22. First demonstration of 200-femtosecond resolution in a GUED instrument.

22. Yang J, Guehr M, Vecchione T, Robinson MS, Li R, et al. 2016. Diffractive imaging of a rotational wavepacket in nitrogen molecules with femtosecond megaelectronvolt electron pulses. *Nat. Commun.* 7:11232

23. Article describes a molecular movie of nonadiabatic molecular dynamics with GUED.

23. Yang J, Zhu X, Wolf TJA, Li Z, Nunes JPF, et al. 2018. Imaging CF_3I conical intersection and photodissociation dynamics with ultrafast electron diffraction. *Science* 361:64–67

24. GUED sheds new light on ring-opening reactions.

24. Wolf TJA, Sanchez DM, Yang J, Parrish RM, Nunes JPF, et al. 2019. The photochemical ring-opening of 1,3-cyclohexadiene imaged by ultrafast electron diffraction. *Nat. Chem.* 11:504–9

25. Wilkin KJ, Parrish RM, Yang J, Wolf TJA, Nunes JPF, et al. 2019. Diffractive imaging of dissociation and ground-state dynamics in a complex molecule. *Phys. Rev. A* 100:023402
26. Liu Y, Horton SL, Yang J, Nunes JPF, Shen X, et al. 2020. Spectroscopic and structural probing of excited-state molecular dynamics with time-resolved photoelectron spectroscopy and ultrafast electron diffraction. *Phys. Rev. X* 10:021016

27. Simultaneous observation of electronic and nuclear dynamics using elastic and inelastic electron scattering.

27. Yang J, Zhu X, Nunes JPF, Yu JK, Parrish RM, et al. 2020. Simultaneous observation of nuclear and electronic dynamics by ultrafast electron diffraction. *Science* 368:885

28. Brockway LO. 1936. Electron diffraction by gas molecules. *Rev. Mod. Phys.* 8:231–66

29. Schomaker V, Glauber ROY. 1952. The Born approximation in electron diffraction. *Nature* 170:290–91
30. Glauber R, Schomaker V. 1953. The theory of electron diffraction. *Phys. Rev.* 89:667–71
31. McClelland JJ, Fink M. 1985. Correlation effects in neon studied by elastic and inelastic high-energy electron scattering. *Phys. Rev. A* 31:1328–35
32. Iijima T, Bonham RA, Ando T. 1963. The theory of electron scattering from molecules. 1. Theoretical development. *J. Phys. Chem.* 67:1472–74
33. Shao H-C, Starace AF. 2010. Detecting electron motion in atoms and molecules. *Phys. Rev. Lett.* 105:263201
34. Shao H-C, Starace AF. 2013. Imaging coherent electronic motion in atoms by ultrafast electron diffraction. *Phys. Rev. A* 88:062711
35. Dixit G, Vendrell O, Santra R. 2012. Imaging electronic quantum motion with light. *PNAS* 109:11636
36. Suominen HJ, Kirrander A. 2014. How to observe coherent electron dynamics directly. *Phys. Rev. Lett.* 112:043002
37. Bennett K, Kowalewski M, Rouxel JR, Mukamel S. 2018. Monitoring molecular nonadiabatic dynamics with femtosecond X-ray diffraction. *PNAS* 115:6538–47
38. Moreno Carrascosa A, Yang M, Yong H, Ma L, Kirrander A, et al. 2021. Mapping static core-holes and ring-currents with X-ray scattering. *Faraday Discuss.* 228:60–81
39. Mott NF, Bragg WL. 1930. The scattering of electrons by atoms. *Proc. R. Soc. Lond. A* 127:658–65
40. Bethe H. 1930. Zur Theorie des Durchgangs schneller Korpuskularstrahlen durch Materie [On the theory of the passage of fast corpuscular rays through matter]. *Ann. Physik* 397:325–400
41. Debye P. 1915. Zerstreuung von Röntgenstrahlen [X-ray scattering]. *Ann. Physik* 351:809–23
42. Prince E. 2004. *International Tables for Crystallography, Volume C: Mathematical, Physical and Chemical Tables*. Dordrecht, Neth.: Kluwer Academic. 3rd ed.
43. Salvat F, Jablonski A, Powell CJ. 2005. ELSEPA—Dirac partial-wave calculation of elastic scattering of electrons and positrons by atoms, positive ions and molecules. *Comput. Phys. Commun.* 165:157–90
44. McClelland JJ, Fink M. 1985. Electron correlation and binding effects in measured electron-scattering cross sections of CO_2. *Phys. Rev. Lett.* 54:2218–21
45. Breitenstein M, Endesfelder A, Meyer H, Schweig A, Zittlau W. 1983. Electron-correlation effects in electron-scattering cross-section calculations of N_2. *Chem. Phys. Lett.* 97:403–9
46. Breitenstein M, Mawhorter RJ, Meyer H, Schweig A. 1984. Theoretical study of potential-energy differences from high-energy electron scattering cross sections of CO_2. *Phys. Rev. Lett.* 53:2398–401
47. Schafer L, Yates AC, Bonham RA. 1971. New values for the partial wave electron scattering factor for the elements $1 \leq Z \leq 57$ and $72 \leq Z \leq 90$ for incident electron energies of 10, 40, 70, and 100 keV. *J. Chem. Phys.* 55:3055–56
48. Schäfer L. 1976. Electron diffraction as a tool of structural chemistry. *Appl. Spectrosc.* 30:123–49
49. Srinivasan R, Lobastov VA, Ruan C-Y, Zewail AH. 2003. Ultrafast electron diffraction (UED). *Helv. Chim. Acta* 86:1761–99
50. Simmermacher M, Henriksen NE, Møller KB, Moreno Carrascosa A, Kirrander A. 2019. Electronic coherence in ultrafast X-ray scattering from molecular wave packets. *Phys. Rev. Lett.* 122:073003
51. Xiong Y, Wilkin KJ, Centurion M. 2020. High-resolution movies of molecular rotational dynamics captured with ultrafast electron diffraction. *Phys. Rev. Res.* 2:043064
52. Baskin JS, Zewail AH. 2005. Ultrafast electron diffraction: oriented molecular structures in space and time. *ChemPhysChem* 6:2261–76
53. Baskin JS, Zewail AH. 2006. Oriented ensembles in ultrafast electron diffraction. *ChemPhysChem* 7:1562–74
54. Reckenthaeler P, Centurion M, Fuß W, Trushin SA, Krausz F, Fill EE. 2009. Time-resolved electron diffraction from selectively aligned molecules. *Phys. Rev. Lett.* 102:213001
55. Centurion M, Reckenthaeler P, Krausz F, Fill E. 2010. Picosecond electron diffraction from molecules aligned by dissociation. *J. Mol. Struct.* 978:141–46
56. Garcia AG, Nahon L, Powis I. 2004. Two-dimensional charged particle image inversion using a polar basis function expansion. *Rev. Sci. Instrum.* 75:4989–96
57. Bartell LS, Gavin RM. 1964. Effects of electron correlation in X-ray and electron diffraction. *J. Am. Chem. Soc.* 86:3493–98

49. Review of the pioneering work of the Zewail group in the development of GUED.

52. Analytical derivation and interpretation of anisotropic GUED diffraction patterns.

57. Theory of inelastic electron and X-ray scattering and their relation to electron correlation.

58. Waller I, Hartree DR, Fowler RH. 1929. On the intensity of total scattering of X-rays. *Proc. R. Soc. Lond. A* 124:119–42
59. Woo YH. 1930. Intensity of total scattering of X-rays by monatomic gases. *Nature* 126:501–2
60. Stapelfeldt H, Seideman T. 2003. *Colloquium*: aligning molecules with strong laser pulses. *Rev. Mod. Phys.* 75:543
61. Mokhtari A, Cong P, Herek JL, Zewail AH. 1990. Direct femtosecond mapping of trajectories in a chemical reaction. *Nature* 348:225–27
62. Yarkony D, Domcke W, Köppel H. 2004. *Conical Intersections: Electronic Structure, Dynamics & Spectroscopy*. London: World Scientific
63. Yarkony DR. 1996. Diabolical conical intersections. *Rev. Mod. Phys.* 68:985–1013
64. Dudek RC, Weber PM. 2001. Ultrafast diffraction imaging of the electrocyclic ring-opening reaction of 1,3-cyclohexadiene. *J. Phys. Chem. A* 105:4167–71
65. Xiong Y, Borne K, Moreno Carrascosa A, Saha SK, Wilkin KJ, et al. 2021. Strong-field induced fragmentation and isomerization of toluene probed by ultrafast femtosecond electron diffraction and mass spectrometry. *Faraday Discuss*. 228:39–59
66. Sanchez A, Amini K, Wang SJ, Steinle T, Belsa B, et al. 2021. Molecular structure retrieval directly from laboratory-frame photoelectron spectra in laser-induced electron diffraction. *Nat. Commun.* 12:1520
67. Blaga CI, Xu J, DiChiara AD, Sistrunk E, Zhang K, et al. 2012. Imaging ultrafast molecular dynamics with laser-induced electron diffraction. *Nature* 483:194–97
68. Wolter B, Pullen MG, Le AT, Baudisch M, Doblhoff-Dier K, et al. 2016. Ultrafast electron diffraction imaging of bond breaking in di-ionized acetylene. *Science* 354:308–12
69. Qi F, Ma Z, Zhao L, Cheng Y, Jiang W, et al. 2020. Breaking 50 femtosecond resolution barrier in MeV ultrafast electron diffraction with a double bend achromat compressor. *Phys. Rev. Lett.* 124:134803
70. Kim HW, Vinokurov NA, Baek IH, Oang KY, Kim MH, et al. 2020. Towards jitter-free ultrafast electron diffraction technology. *Nat. Photonics* 14:245–49
71. Maxson J, Cesar D, Calmasini G, Ody A, Musumeci P, Alesini D. 2017. Direct measurement of sub-10 fs relativistic electron beams with ultralow emittance. *Phys. Rev. Lett.* 118:154802
72. Otto MR, René de Cotret LP, Stern MJ, Siwick BJ. 2017. Solving the jitter problem in microwave compressed ultrafast electron diffraction instruments: robust sub-50 fs cavity-laser phase stabilization. *Struct. Dyn.* 4:051101
73. Wytrykus D, Centurion M, Reckenthaeler P, Krausz F, Apolonski A, Fill E. 2009. Ultrashort pulse electron gun with a MHz repetition rate. *Appl. Physics B* 96:309–14
74. Filippetto D, Qian H. 2016. Design of a high-flux instrument for ultrafast electron diffraction and microscopy. *J. Phys. B* 49:104003
75. Abbamonte P, Abild-Pedersen F, Adams P, Ahmed M, Albert F, et al. 2015. *New science opportunities enabled by LCLS-II X-ray lasers*. US Dept. Energy Tech. Rep., SLAC Natl. Accel. Lab., Menlo Park, CA
76. van Oudheusden T, Pasmans PLEM, van der Geer SB, de Loos MJ, van der Wiel MJ, Luiten OJ. 2010. Compression of subrelativistic space-charge-dominated electron bunches for single-shot femtosecond electron diffraction. *Phys. Rev. Lett.* 105:264801